Supplement of Mech. Sci., 17, 857–871, 2026
https://doi.org/10.5194/ms-17-857-2026-supplement

mechanical sciences

Supplement of

Shaft-flexibility-induced hydrodynamic support redistribution and modal response in a multi-support bearing-rotor system

Yulin Zhang et al.

Correspondence to: Bing Li (gxgxyjxxlb@163.com)

S1 Definition, calibration, and robustness of M_r

The flexible-deformation index M_r compresses the journal-centre eccentricity and the additional edge displacement induced by journal inclination into a dimensionless descriptor. It is used solely to post-process a converged FSI state and is not an additional physical parameter in either the Reynolds equation or the rotordynamic equations. The index is defined as follows:

$$M_r = \sqrt{\varepsilon^2 + \left(\lambda \frac{L_b}{2C} \tan\gamma_i\right)^2} \tag{S1}$$

Here, ε is the eccentricity ratio, L_b is the bearing length, C is the radial clearance, and γ is the journal-centreline inclination. The weighting coefficient λ balances the scales of the eccentricity and inclination terms only. It does not enter the Reynolds equation, the FSI equilibrium, the extraction of oil-film stiffness and damping coefficients, or the rotordynamic eigenvalue problem. Changing λ therefore changes the numerical representation of a fixed physical state on the M_r coordinate, but not the underlying solution.

To avoid selecting λ entirely by experience, we constructed a statistical reference by balancing the root-mean-square (RMS) magnitudes over the full operating domain. This procedure gave λ_{RMS} = 2.3545. A 1000-sample bootstrap over physical load-speed clusters yielded a 95% confidence interval of 2.3486-2.3603, indicating stable sampling behaviour. The support-specific RMS reference weights differed appreciably, confirming that a single global coefficient is a system-level compromise rather than a local optimum for every support.

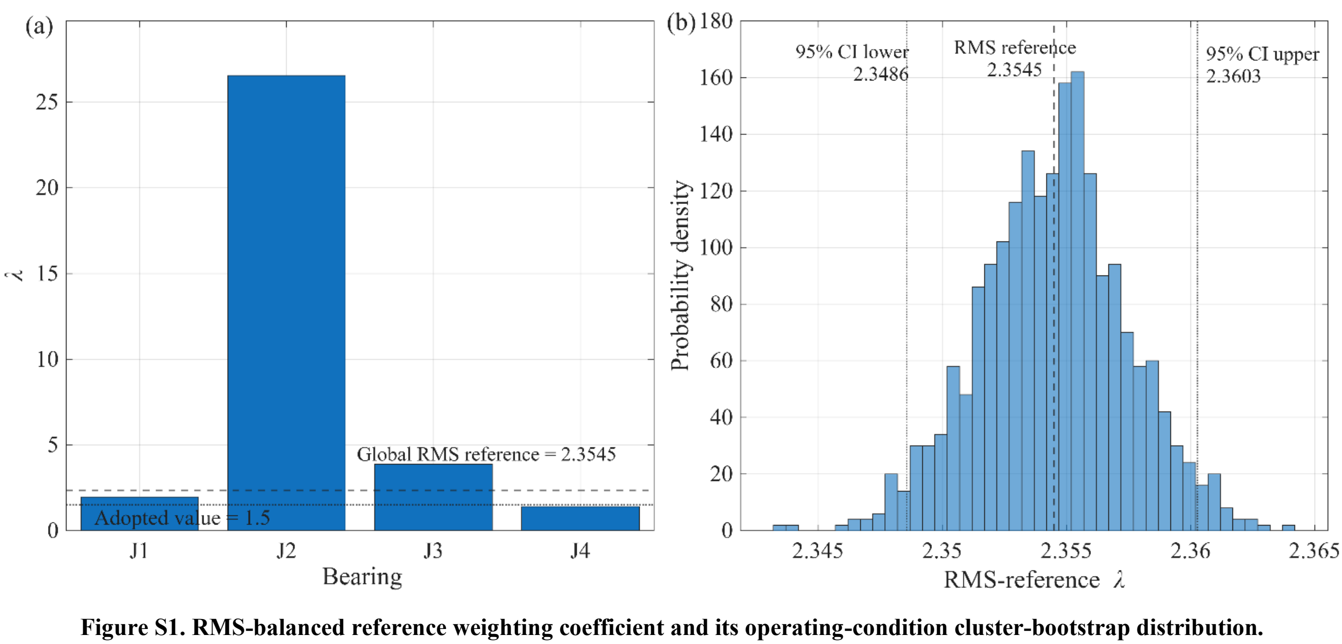

Figure S1. RMS-balanced reference weighting coefficient and its operating-condition cluster-bootstrap distribution.

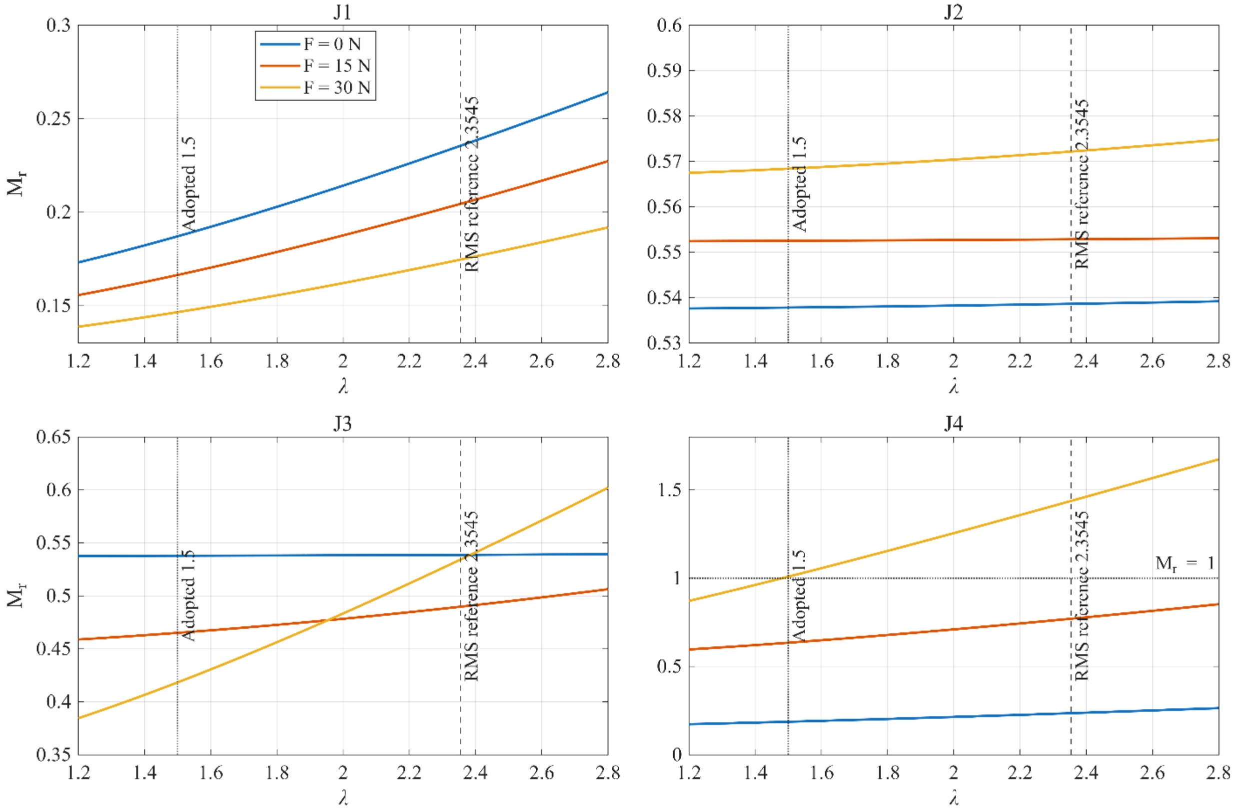

Figure S2. Variation of M_r with the weighting coefficient λ for fixed physical states at 3000 *rpm*.

Figure S2 compares M_r as λ varies while the physical states at 3000 *rpm* remain fixed. J_2 was least sensitive to the weighting coefficient, J_1 showed moderate sensitivity, and the sensitivities of J_3 and J_4 increased under high load, with the largest response at J_4. Applying λ_{RMS} increased M_r at the high-load J_4 states and extended the original compact interpretation scale near $O(1)$.

Table S1. Sensitivity of M_r to the weighting coefficient under fixed physical operating conditions.

Rotational speed (*rpm*)	*F* (*N*)	Bearing	M_r (λ = 1.5)	M_r (λ_{RMS} = 2.3545)	Relative change (%)	Ranking changed
2884	0	J1	0.1912	0.2386	24.79	No
2884	0	J2	0.5481	0.5489	0.15	No
2884	0	J3	0.5481	0.5489	0.15	No
2884	0	J4	0.1912	0.2386	24.79	No
2884	15	J1	0.1704	0.2075	21.78	No
2884	15	J2	0.5626	0.5629	0.06	No
2884	15	J3	0.4752	0.4994	5.09	No
2884	15	J4	0.6427	0.7773	20.94	No
2884	30	J1	0.1504	0.1776	18.14	No
2884	30	J2	0.5784	0.5821	0.64	No
2884	30	J3	0.4254	0.5398	26.88	No
2884	30	J4	1.0089	1.4379	42.52	No
3000	0	J1	0.1871	0.2356	25.88	No

Rotational speed (*rpm*)	*F* (*N*)	Bearing	M_r (λ = 1.5)	M_r (λ_{RMS} = 2.3545)	Relative change (%)	Ranking changed
3000	0	J2	0.5378	0.5387	0.15	No
3000	0	J3	0.5378	0.5387	0.15	No
3000	0	J4	0.1871	0.2356	25.88	No
3000	15	J1	0.1665	0.2045	22.87	No
3000	15	J2	0.5525	0.5529	0.06	No
3000	15	J3	0.4651	0.4898	5.31	No
3000	15	J4	0.6346	0.7706	21.44	No
3000	30	J1	0.1466	0.1747	19.18	No
3000	30	J2	0.5684	0.5722	0.66	No
3000	30	J3	0.4183	0.5343	27.72	No
3000	30	J4	1.0087	1.4378	42.54	No

Across all fixed states at 2884 and 3000 *rpm*, changing λ from 1.5 to λ_{RMS} altered the magnitude of M_r but never changed the J_1-J_4 ranking. J_1 still decreased with load, J_2 remained comparatively stable, J_3 retained its transitional response, and the loaded-end support J_4 strengthened markedly. We therefore retained λ = 1.5 as the reporting coefficient and used λ_{RMS} only as an independent sensitivity reference. The inferred hydrodynamic support redistribution and loaded-end dominance do not depend on a particular choice of λ.

S2 Applicability of the small-deformation assumption and assessment of geometric nonlinearity

S2.1 Structural assumption and validation strategy

The shaft is represented by a Timoshenko beam model that resolves transverse bending and shear deformation. Its structural stiffness matrix is constructed in the reference configuration; hence, the structural formulation assumes small strain and small rotation and does not explicitly include the second-order axial elongation produced by large deflection or its configuration-dependent geometric stiffness. Journal eccentricity and inclination nevertheless remain state-dependent in the lubrication geometry, and the oil-film pressure, reaction forces, and dynamic coefficients are updated at every converged FSI state. The model is therefore geometrically linear in the structure, state-dependent at the lubrication boundary, and locally linearised for small perturbations about equilibrium.

For transverse displacements $u(z)$ and $v(z)$, the lowest-order axial elongation generated by bending in a von Kármán-type kinematic relation is

$$\varepsilon_g^2 = \frac{1}{2}\left[\left(\frac{\partial u}{\partial z}\right)^2 + \left(\frac{\partial v}{\partial z}\right)^2\right] \tag{S2}$$

At each bearing section, the centreline-slope components are denoted by S_x and S_y, and the corresponding inclination satisfies

$$\tan\gamma = \sqrt{S_x^2 + S_y^2} \tag{S3}$$

The following quantity can therefore be used as an a posteriori indicator of the lowest-order geometric-nonlinearity correction:

$$\varepsilon_g^2 = \frac{1}{2}\tan^2\gamma \tag{S4}$$

We evaluated the assumption at two levels. First, all directly converged FSI states were screened for their actual centreline inclinations and second-order geometric terms. Second, a deliberately conservative, fully axially restrained upper-bound model was constructed and compared with the linear structural model for the *FW*, *BW*, *H1*, and *H2* synchronous branches.

S2.2 Working-domain kinematic check

The offline database spans F = 0-30 N and n = 1000-8000 rpm and contains 211001 load-speed states. Of these, 200304 states converged directly in the original FSI calculations, corresponding to 94.93% of the database. Only states with $success_{\text{map}} = 1$ were used in the present physical assessment; values introduced later to fill missing database entries were not treated as independent physical states. Using λ = 1.5, L_b = 11 mm, and C = 15 μm gives $\lambda L_b/(2C) = 550$, and Eq. (S1.1) can then be inverted to recover the actual centreline slope. No directly converged state produced the following nonphysical condition beyond numerical tolerance:

$$M_r^2 < \varepsilon^2 \tag{S5}$$

The relative error associated with the small-angle approximation tan $\gamma \approx \gamma$ was evaluated from

$$e_{\tan} = \frac{|\tan\gamma - \gamma|}{|\tan\gamma|} \times 100\% \tag{S6}$$

Table S2. Principal indicators used to assess the small-deformation assumption.

Metric	Maximum value	Operating condition	Controlling location
Maximum centreline inclination $\gamma_{\max}$	0.0886889°	F = 30 N, 8000 rpm	J_4
Maximum centreline slope tan γ	1.5479×10^{-3}	Same as above	J_4
Second-order geometric-elongation proxy 1/2 tan² γ	1.1980×10^{-6}	Same as above	J_4
Relative error in tan $\gamma \approx \gamma$	Approximately 7.99×10^{-5}%	State of the same extreme order	J_4
Directly converged states	200304	—	—
Fraction of directly converged states	94.93%	—	—

The maximum centreline inclination was 0.0886889° at J_4 for F = 30 N and 8000 rpm. Its second-order geometric-elongation proxy was only 1.1980×10^{-6}, and the worst relative error in tan $\gamma \approx \gamma$ was approximately 7.99×10^{-5}%. An inclination that is important to a micrometre-scale oil film is therefore not equivalent to a large structural rotation of the metre-scale shaft.

S2.3 Branch-specific kinematic check

The FW, BW, $H1$, and $H2$ states used in the synchronous-branch analysis were checked separately so that the database-wide statistics could be linked directly to the reported modal results.

Table S3. Structural inclination scales at the low- and high-flexibility states of the four synchronous branches.

Branch	State	F (N)	Critical speed (rpm)	Maximum γ (°)	$1/2\tan^2\gamma$	Maximum angular error (%)
FW	Low	0	2883.6771	0.0122894	2.3003×10^{-8}	1.5335×10^{-6}
FW	High	30	2883.6665	0.0882119	1.1852×10^{-6}	7.9011×10^{-5}
BW	Low	0	2894.9847	0.0122926	2.3015×10^{-8}	1.5343×10^{-6}
BW	High	30	2894.9960	0.0882122	1.1852×10^{-6}	7.9012×10^{-5}
$H1$	Low	0	4819.5	0.0126725	2.4460×10^{-8}	1.6306×10^{-6}
$H1$	High	30	4820.1	0.0883867	1.1899×10^{-6}	7.9325×10^{-5}
$H2$	Low	0	5080.9	0.0127069	2.4592×10^{-8}	1.6395×10^{-6}
$H2$	High	30	5088.5	0.0884167	1.1907×10^{-6}	7.9378×10^{-5}

At the high-flexibility states, the maximum inclinations were 0.0882°-0.0884°, close to the database-wide maximum of 0.08869°, while the corresponding second-order terms remained near 1.19×10^{-6}. Would a correction of this scale materially alter the reported synchronous branches? To answer that question directly, we imposed a conservative stress-stiffening upper bound rather than relying on the angular scale alone.

S2.4 Conservative stress-stiffening upper bound

If the second-order elongation represented by Eq. (S4) is assumed to be fully restrained axially, the associated tensile-force upper bound is

$$N_g^{ub} = EA\varepsilon_g^{(2)} \tag{S7}$$

Substitution of the model parameters gives the deliberately conservative value

$$N_g^{ub} = 23.45N \tag{S8}$$

This value is not an actual axial force in the system. It is conservative because the maximum local second-order elongation near a bearing section is assumed to act uniformly along the full 1.2 m shaft and is then assumed to be completely prevented. Real multi-support journal-bearing rotors do not satisfy either extreme condition. The complete non-symmetric oil-film stiffness and damping matrices and the gyroscopic matrix were left unchanged and continued to be interpolated at the actual synchronous-root speed. The check therefore changed only the structural stress-stiffening level.

Table S4. Branch-specific geometric-stiffness upper-bound results evaluated at each high-flexibility state.

Branch	N_g^{ub} (N)	Critical-speed change (%)	Endpoint $cMAC$	Minimum consecutive $cMAC$	Maximum mode-envelope difference
FW	23.2018	+0.10098	0.99999825	0.999999996	0.000997
BW	23.2020	+0.09896	0.99999888	0.999999997	0.000951

Branch	N_g^{ub} (*N*)	Critical-speed change (%)	Endpoint *cMAC*	Minimum consecutive *cMAC*	Maximum mode-envelope difference
H1	23.2939	+0.07719	0.99999996	0.9999999999	0.001326
H2	23.3097	+0.07375	0.99999995	0.9999999999	0.001450

A second calculation used the uniform upper bound associated with the maximum inclination in the entire database.

Table S5. Synchronous-branch response under the most adverse database-wide geometric-stiffness upper bound.

Branch	Linear critical speed (*rpm*)	Critical-speed change (%)	Endpoint *cMAC*	Minimum consecutive *cMAC*	Maximum mode-envelope difference
FW	2883.6664	+0.10207	0.99999821	0.999999996	0.001008
BW	2894.9959	+0.10003	0.99999886	0.999999997	0.000962
H1	4820.1409	+0.07772	0.99999996	0.9999999999	0.001335
H2	5088.4546	+0.07420	0.99999995	0.9999999999	0.001459

Even under the fully restrained stress-stiffening bound, the largest relative critical-speed change among the four branches was only 0.1021%. All endpoint *cMAC* values exceeded 0.999998, and the maximum difference between normalised spatial-mode envelopes was below 0.00146. Thus, the conservative correction neither materially shifted the synchronous critical speeds nor reconstructed the reported modes.

S2.5 Interpretation and applicability boundary

The kinematic and dynamic checks reveal a clear separation of scales. Shaft deformation is sufficiently large relative to the radial clearance and film thickness to change the hydrodynamic boundary, yet the corresponding rotation remains small relative to the global shaft geometry. A full large-deflection structural theory is therefore not required within the investigated domain. This conclusion should not be extrapolated to systems with much larger shaft deflection or rotation, strong axial restraint or axial load, rubbing contact, local buckling, or large-amplitude transient vibration, for which configuration-dependent geometric stiffness may become important.

S3 Lubrication-model assumptions, sensitivity, and applicability limits

The finite-length hydrodynamic journal bearing is described by an isothermal, constant-viscosity, laminar Reynolds equation, with negative pressure in the divergent region truncated by a half-Sommerfeld condition. The formulation is used for the static FSI equilibrium and for the linearised oil-film dynamic coefficients in its neighbourhood. The checks below distinguish the robust direction and ordering of hydrodynamic support redistribution from local magnitudes that remain sensitive to thermal, cavitation, and lubrication-regime assumptions.

S3.1 Laminar-flow and full-film screening

The clearance-scale Reynolds number was defined as $R_{eC} = \rho UC/\mu$, where $U = \Omega R$. Representative low-, intermediate-, and high-load states were screened using ρ = 850 $kg\ m^{-3}$, C = 15 μm, and μ = 0.017 $Pa\ s$. Full-film operation was assessed conservatively using $\Lambda = h_{\min} \Big/ \sqrt{R_{q,j}^2 + R_{q,b}^2}$, with $R_{q,j}$ = 0.5 μm and $R_{q,b}$ = 1.0 μm, giving a composite roughness of 1.118 μm. A value of $\Lambda > 3$ was used as a screening threshold; $\Lambda < 3$ indicates that asperity contact cannot be excluded, not that contact has been demonstrated.

Table S6. Laminar-flow and full-film screening at representative operating conditions.

Case	F (N)	Rotational speed (rpm)	Most adverse support	$h_{\min}$ (μm)	R_{eC}	Λ	Assessment
L	5	1500	J_2	4.410	0.648	3.944	Laminar/full-film screens passed
M	15	3000	J_4	4.719	1.296	4.220	Laminar/full-film screens passed
H	27	4500	J_4	1.739	1.944	1.556	Laminar screen passed; mixed-lubrication effects require assessment

The largest representative R_{eC} was only 1.944, far below the screening threshold of 1000, supporting the laminar-flow assumption throughout the investigated domain. The low and intermediate cases passed the full-film screen. In the high-load case, J_1-J_3 remained within the full-film range, whereas Λ at J_4 fell to 1.556. Consequently, local pressure and dynamic-coefficient magnitudes at the limiting H-J_4 state may be affected by asperity contact or mixed lubrication.

S3.2 Equivalent-viscosity sensitivity

Because the energy equation is not solved, the model cannot directly predict a thermohydrodynamic temperature field. We instead used equivalent-viscosity changes as a proxy for plausible thermal effects. At each fixed load and speed, the dynamic viscosity was set to $0.8\mu_0$, $1.0\mu_0$, and $1.2\mu_0$, where μ_0 = 0.017 $Pa\ s$. The complete four-support FSI equilibrium and all K/C matrices were recomputed at each viscosity; the baseline coefficients were not scaled algebraically.

Table S7. Complete FSI sensitivity results for equivalent-viscosity variations of ±20%.

Case	μ/μ_0	μ ($Pa{\cdot}s$)	Minimum h (μm)	Maximum P (MPa)	Maximum K-matrix change (%)	Maximum C-matrix change (%)	Dominant support
L	1.0	0.0170	4.420	0.608	0	0	J2
L	0.8	0.0136	3.766	0.645	15.50	13.98	J2
L	1.2	0.0204	4.990	0.580	14.90	14.28	J2
M	1.0	0.0170	4.725	0.537	0	0	J2
M	0.8	0.0136	3.797	0.568	18.73	18.48	J2
M	1.2	0.0204	5.509	0.517	18.93	18.77	J2
H	1.0	0.0170	1.731	1.355	0	0	J4
H	0.8	0.0136	1.002	1.853	22.14	19.48	J4
H	1.2	0.0204	2.397	1.155	19.56	19.50	J4

Across the non-baseline calculations, the maximum changes in the stiffness and damping matrices reached 22.14% and 19.50%, respectively. The largest changes in minimum film thickness and peak pressure were 42.16% and 36.78%. Constant viscosity therefore affects the precise local magnitudes in the limiting thin-film state and cannot be described as negligible. Nevertheless, J_2 remained the dominant support in the low and intermediate cases, J_4 remained dominant in the high-load/high-speed case, and the *K/C* ordering and signs were preserved. Equivalent-viscosity changes modified absolute values without changing the nonuniform redistribution or the shift of the controlling support.

Table S8. Film-thickness ratios at the most adverse support for each viscosity level.

Case	Λ ($0.8\mu_0$)	Λ ($1.0\mu_0$)	Λ ($1.2\mu_0$)	Interpretation
L	3.37	3.95	4.46	Full-film screen passed at all viscosity levels
M	3.40	4.23	4.93	Full-film screen passed at all viscosity levels
H	0.90	1.55	2.14	All three values are below 3; H-J4 is a limiting state

S3.3 Squeeze contribution, cavitation treatment, and integrated boundary

A statement that transient squeeze is entirely omitted would be inaccurate. The journal attitude is time-independent in the static FSI equilibrium, so no finite-amplitude transient squeeze arises in that calculation. During dynamic-coefficient extraction, however, positive and negative dimensionless velocity perturbations activate the film-thickness time-derivative term in the Reynolds equation. The damping matrix is obtained by central differences of the oil-film force with respect to velocity. First-order velocity-dependent squeeze reaction is therefore retained in *C*.

The model does not include nonlinear time-dependent squeeze along a finite-amplitude journal orbit, pressure-history effects, moving cavitation boundaries, reformation after film rupture, start-stop transients, impact, or large-amplitude nonlinear vibration. Because the subsequent complex-eigenvalue, Campbell-diagram, and local *K*/*C* analyses concern small perturbations about equilibrium, the retained first-order squeeze contribution is consistent with the study objective, but the conclusions do not extend to those strongly transient processes.

The half-Sommerfeld treatment sets negative pressure in the divergent region to zero but does not enforce mass conservation in the cavitated zone; it is therefore not equivalent to a JFO or Elrod-Adams formulation. Pressure validation showed close agreement with reference results for γ = 0-0.007°. At γ = 0.010°, the present peak was 371.3 *MPa*, compared with 409.8-414.8 *MPa* in the references, a difference of approximately 9%-11%. This limiting state combines severe local film thinning with increased sensitivity to grid resolution, viscosity, and cavitation-boundary treatment.

Taken together, the direction and ordering of hydrodynamic support redistribution are robust: the representative states are clearly laminar, the controlling-support ranking is unchanged under ±20% equivalent-viscosity variation, and the J_2-to-J_4 shift persists. By contrast, the exact peak pressure, minimum film thickness, 4298% stiffness-trace increase, and extreme *K*/*C* magnitudes at J_4 remain predictions of the present isothermal, laminar, nominally full-film, non-mass-conserving cavitation model. Direct comparisons with mass-conserving cavitation, thermohydrodynamic, or mixed-lubrication formulations are required before those limiting magnitudes can be generalised.

S4 Numerical verification of the FSI and database-assisted workflow

The production database spans F = 0-30 N and n = 1000-8000 rpm with ΔF = 0.1 N and Δn = 10 rpm, giving 301×701 = 211001 load-speed states. Each state preserves the identities of J_1-J_4 and stores the equilibrium variables and complete 2×2 stiffness and damping matrices for every support. M_r is stored only as a post-processing descriptor and is not an interpolation coordinate.

Table S9. Production database and baseline numerical settings.

Item	Production setting
End-load grid	0-30 N, ΔF = 0.1 N, 301 points
Rotational-speed grid	1000-8000 rpm, Δn = 10 rpm, 701 points
Number of load-speed states	211001
Supports	Complete K/C matrices stored separately for J_1-J_4
Production Reynolds grid	61×81 (circumferential×axial)
Baseline dimensionless perturbation for dynamic coefficients	$\delta = 10^{-4}$ (centred differences for displacement and velocity)
FSI relative-residual tolerance	10^{-5}
Absolute free-DOF residual check	10^{-10} N
Auxiliary closure residual	$\lvert g \rvert < 10^{-6}$
Relaxation factor/maximum allowed iterations	0.4 / 200

S4.1 Reynolds-grid independence

Grid independence was assessed using 41×61, 61×81, and 81×101 circumferential-axial grids at the L (5 N, 1500 rpm), M (15 N, 3000 rpm), and H (27 N, 4500 rpm) operating conditions. Recomputing the four-support FSI equilibrium and the dynamic coefficients produced 12 valid support states for each grid. Matrix errors were measured with the relative Frobenius norm against the 81×101 grid.

Table S10. Reynolds-grid convergence results, with 81×101 used as the reference.

Grid	Valid results	Mean time (s)	Mean K error (%)	Maximum K error (%)	Mean C error (%)	Maximum C error (%)	Maximum ε error (%)	Maximum M_r error (%)
41×61	12	44.65	1.558	4.138	2.169	7.053	0.196	0.165
61×81 (production)	12	145.62	1.194	3.860	1.736	6.441	0.050	0.034
81×101 (reference)	12	347.62	0	0	0	0	0	0

With the 61×81 grid, the mean K- and C-matrix errors were 1.194% and 1.736%, and their maxima were 3.860% and 6.441%. The maximum errors in ε and M_r were only 0.050% and 0.034%. Refining to 81×101 increased the mean time per operating state from 145.62 s to 347.62 s, a factor of approximately 2.39. The 61×81 grid was retained as an accuracy-cost compromise. Individual cross-coupled damping or high-gradient coefficients can have errors above the mean, so the production grid is not claimed to be strictly equivalent to the finest grid; it does, however, recover the equilibrium state and the trend of multi-support coefficient redistribution consistently.

S4.2 Perturbation-scale sensitivity

The stiffness and damping matrices were obtained by centred differences with dimensionless displacement and velocity perturbations. The production value was $\delta = 10^{-4}$. Each perturbation was varied independently from 0.25 to 4 times its baseline while the other perturbation was held fixed.

Table S11. Sensitivity of the dynamic coefficients to perturbation size.

Test	Factor relative to baseline	Maximum *K* error (%)	Maximum *C* error (%)	*K* sign agreement (%)	*C* sign agreement (%)
Displacement perturbation	0.25	0.0385	0	100	100
Displacement perturbation	0.50	0.0332	0	100	100
Displacement perturbation	1.00	0	0	100	100
Displacement perturbation	2.00	0.0576	0	100	100
Displacement perturbation	4.00	0.1217	0	100	100
Velocity perturbation	0.25	0	0.0724	100	100
Velocity perturbation	0.50	0	0.0617	100	100
Velocity perturbation	1.00	0	0	100	100
Velocity perturbation	2.00	0	0.0661	100	100
Velocity perturbation	4.00	0	0.0718	100	100

The largest stiffness-matrix change over the displacement scan was 0.1217%, and the largest damping-matrix change over the velocity scan was 0.0724%. Every *K*/*C* component retained its sign. Thus, $\delta = 10^{-4}$ lies within a stable centred-difference range, and the pronounced J_4 stiffness increase is not an artefact of the perturbation size.

S4.3 FSI convergence assessment

Let Rf denote the force-equilibrium residual at the free structural degrees of freedom and f_{ext},f the external-load vector restricted to those degrees of freedom. The normalised residual used in the database calculations is

$$r_{rel}^{(k)} = \frac{\left\| R_f^{(k)} \right\|}{\max\left(\left\| f_{ext,f} \right\|, 10^{-6} \right)} \tag{S9}$$

Table S12. Numerical settings and convergence criteria used in the FSI equilibrium iteration.

Quantity	Value/definition	Role
Normalized residual	$r_{rel} = \|\|R_f\|\|^2 / \max(\|\|f_{ext},f\|\|^2, 10^{-6})$	Primary normalized equilibrium monitor
Relative tolerance	10^{-5}	Database calculation tolerance
Absolute residual threshold	$\|\|R_f\|\|^2 < 10^{-10}\ N$	Additional stringent internal check
Auxiliary closure criterion	$\|g\| < 10^{-6}$	Additional equilibrium-closure check
Relaxation factor	0.4	Damped state update
Maximum iterations	200	Upper limit for one equilibrium solve

Table S13. Convergence characteristics of four representative FSI equilibrium states.

Case	F (N)	Speed (rpm)	First $r_{rel} < 10^{-5}$	Coupled criterion	Strict stop	Total iterations	Final r_{rel}	Final $\|\|R_f\|\|_2$ (N)	Final $\|g\|$
C1	0	2884	25	36	55	55	2.729×10^{-12}	8.507×10^{-11}	6.035×10^{-11}
C2	15	2884	25	36	56	56	2.838×10^{-12}	9.823×10^{-11}	4.659×10^{-11}
C3	30	2884	34	43	—	200	3.068×10^{-12}	1.328×10^{-10}	8.450×10^{-12}
C4	30	3000	34	45	—	200	2.674×10^{-12}	1.157×10^{-10}	1.005×10^{-12}

Only after $r_{rel} < 10^{-5}$ and $|g| < 10^{-6}$ were returned states classified as satisfying the coupled criterion; the strict internal stop additionally required $||R_f||_2 < 10^{-10}$ N. C1 and C2 met the coupled criterion after 36 iterations and the strict stop after 55 and 56 iterations. C3 and C4 met the coupled criterion after 43 and 45 iterations, respectively. Their absolute residuals then approached a numerical floor near 10^{-10} N rather than exhibiting growth in the normalised equilibrium residual.

An additional diagnostic grid used $F = \{0, 10, 20, 30\}$ N and speeds from 1000 to 8000 rpm in increments of 1000 rpm, giving 32 operating points. Twenty-seven points returned valid hydrodynamic equilibrium states with recorded iteration histories. All 27 met the coupled criterion, and 26 also met the strict internal stop.

Table S14. Summary statistics for the 32-point coarse load-speed convergence diagnostic.

Metric	Result
Operating points tested	32
Valid hydrodynamic solutions returned	27 / 32
Returned states satisfying coupled criterion	27 / 27 (100%)
Returned states satisfying strict internal stop	26 / 27
Returned states reaching maxIter	1 / 27
Mean iterations to coupled criterion	35.70
Median iterations to coupled criterion	35
95th percentile	39.7
Maximum iterations to coupled criterion	45
Mean strict-stop iteration (strictly converged states)	60.92
Median strict-stop iteration (strictly converged states)	55.5
Maximum strict-stop iteration (strictly converged states)	109

Table S15. First iteration satisfying the coupled criterion over the coarse load-speed grid; NR denotes no valid hydrodynamic equilibrium state returned.

F (N)	1000	2000	3000	4000	5000	6000	7000	8000
0	NR	37	35	35	34	34	33	32
10	NR	37	36	35	35	34	33	33
20	NR	39	37	36	35	34	34	34
30	NR	NR	45	40	38	37	36	36

The maximum observed iteration count required to meet the coupled criterion was 45, whereas 200 was the configured upper limit for a single equilibrium solve. These quantities describe different aspects of the algorithm and must not be conflated. The five NR points were excluded from convergence statistics because the recorded solver history identified only NaN/Inf termination and did not support attribution to a specific lubrication mechanism.

S4.4 Off-grid interpolation accuracy and treatment of nonconvergent states

To avoid coinciding with database nodes, 12 combinations were formed from $F = 4.55$, 14.55, and 27.55 N and $n = 1455$, 2885, 4355, and 5855 rpm. Direct FSI results were compared independently with bilinear interpolation for the complete 2×2 K/C matrices at J1-J4. The direct calculation at $F = 27.55$ N and 1455 *rpm* did not return usable dynamic coefficients; the remaining 11 system states yielded 44 valid support matrices. Every interpolation point included in the error statistics was surrounded by four directly converged database corners.

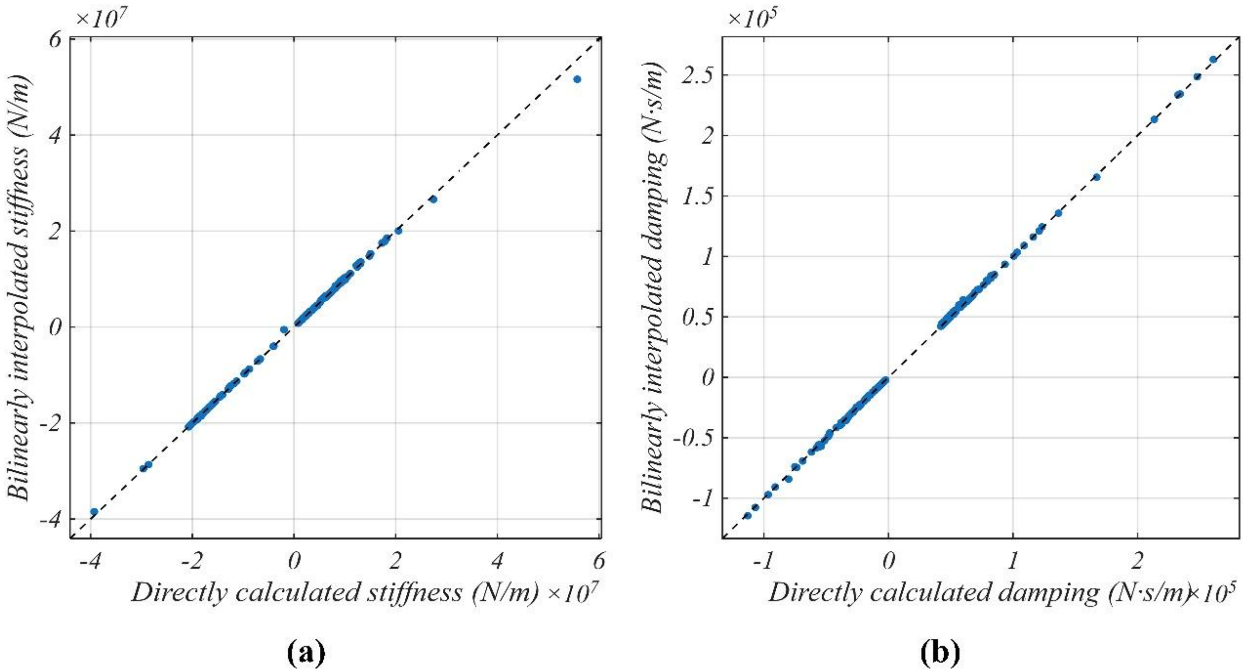

Figure S3. Bearing dynamic coefficients obtained by direct calculation and bilinear interpolation: (a) stiffness; (b) damping.

Table S16. Bilinear-interpolation errors for the bearing dynamic-coefficient matrices.

Matrix	Valid samples	Mean error (%)	Median error (%)	P95 error (%)	Maximum error (%)
K	44	1.82	1.70	2.74	6.36
C	44	1.43	1.37	2.52	2.88

Table S17. Off-grid interpolation error statistics for individual dynamic coefficients.

Dynamic coefficient	NRMSE (%)	R^2	Sign agreement (%)
Kxx	2.14	0.9981	100
Kxy	4.14	0.9916	100
Kyx	0.89	0.9995	100
Kyy	5.14	0.9954	100
Cxx	2.83	0.9775	100
Cxy	2.21	0.9988	100
Cyx	1.88	0.9991	100
Cyy	0.46	0.9999	100

Table S18. Matrix interpolation errors at the four supports.

Support	Mean *K* (%)	*K P*95 (%)	Maximum *K* (%)	Mean *C* (%)	*C P*95 (%)	Maximum *C* (%)
J_1	1.74	2.67	2.68	1.30	2.15	2.18
J_2	1.58	2.27	2.27	1.51	2.68	2.88
J_3	1.67	2.20	2.20	1.19	1.65	1.66
J_4	2.28	4.64	6.36	1.72	2.57	2.62

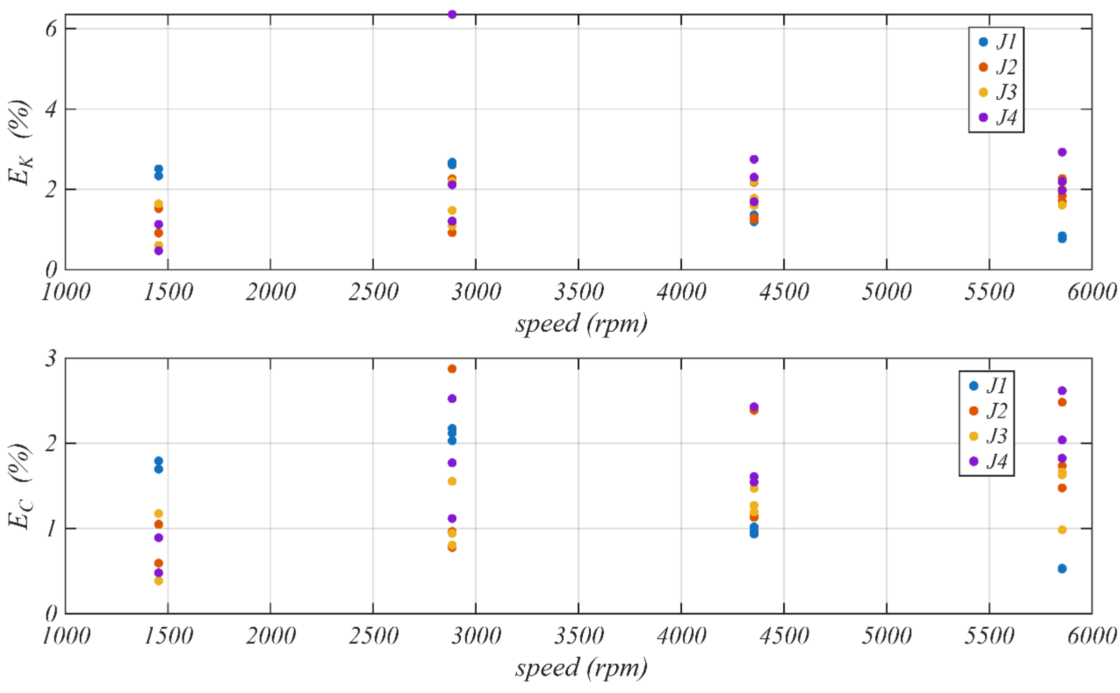

Figure S4. Off-grid interpolation errors of the bearing dynamic-coefficient matrices at J_1-J_4.

Of the 211001 production states, 200304 were returned directly by the original FSI solver, corresponding to 94.93%. The $success_{map}$ preserves this direct-solution status before any missing-value processing. States with $success_{map} = 0$, NaN/Inf values, or no valid equilibrium are excluded from grid, extreme-value, convergence-rate, and independent-validation statistics. Linear interpolation, with nearest-neighbour filling at the boundary, is used only to maintain continuity for online *K/C* lookup; filled states are not described as directly converged physical operating points.

S5 Hierarchical validation of the multi-support coupled model

Validation was organised into four independent levels: local oil-film pressure, oil-film dynamic coefficients, structural rotor modes, and database interpolation. This hierarchy does not constitute a complete experimental calibration of the target three-disc, four-support apparatus. It does, however, test the principal numerical modules of the coupling chain and provides an off-grid direct-solution check of the database-assisted system analysis.

Table S19. Hierarchical validation and the associated evidential boundaries.

Validation level	Reference	Result	Scope
Local lubrication pressure	Sun and Gui (2004), Lv et al. (2018)	Peak-pressure trends agree for γ = 0-0.007°; at γ = 0.010°, the present value is 371.3 *MPa*, approximately 9%-11% below the references	Checks the main pressure trend for a misaligned finite-length bearing and exposes the sensitivity of the limiting thin-film state to cavitation, grid, and model assumptions
Stiffness and damping coefficients	Dimensionless K/C data of Lund and Orcutt (1967)	The stiffness and damping curves agree overall, with consistent coefficient signs and principal trends	Checks perturbation-based coefficient extraction and scale recovery
Structural rotor model	High-fidelity ANSYS finite-element model at 3000 *rpm* and *F* = 0 *N*	The normalised modes near 53 and 89 Hz reproduce the support-adjacent nodes and disc-location peaks, with only small local amplitude differences	Independently checks the Timoshenko-beam structural modes; it does not validate the oil-film coupling itself
Database interpolation	Direct FSI solutions at 12 off-grid points	*K*-matrix mean/*P*95/maximum errors: 1.8178%/2.7369%/6.3579%; *C*-matrix errors: 1.4309%/2.5205%/2.8781%	Directly checks the numerical accuracy of offline-database to online-bilinear-interpolation transfer in the multi-support analysis

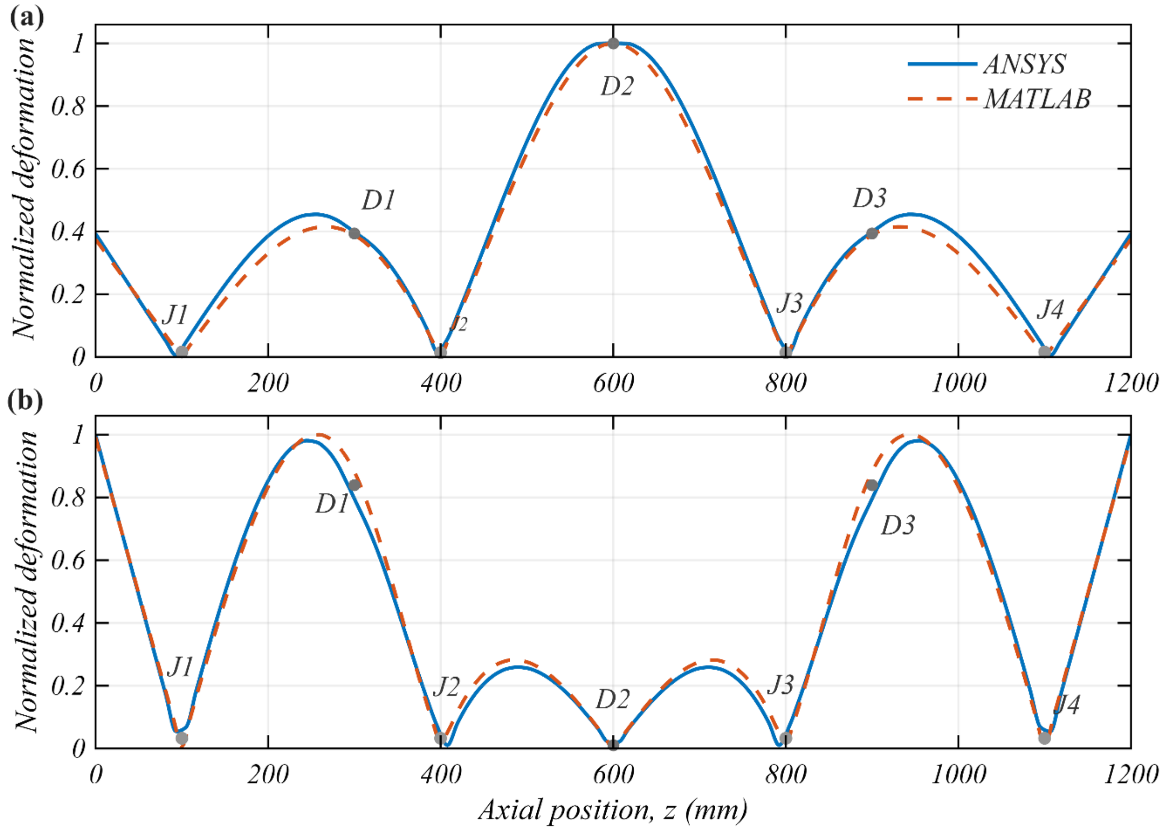

Figure S5. Normalised bending modes obtained with the MATLAB and ANSYS models: (a) mode near 53 *Hz*; (b) mode near 89 *Hz*.

For the structural check, normalised bending modes obtained from the MATLAB Timoshenko beam model were compared with an ANSYS three-dimensional finite-element model at 3000 *rpm* and $F = 0$ *N*. The modes near 53 and 89 *Hz* showed consistent nodal positions near the supports and peak locations at the discs, with only minor local amplitude differences.

Maximum oil-film pressure was compared with Sun and Gui (2004) and Lv et al. (2018) under journal inclination. The normal and moderately inclined states agreed closely, while the limiting $\gamma = 0.010°$ state exposed the model dependence discussed in Sect. S3.

Table S20. Comparison of maximum oil-film pressure under journal inclination.

Inclination angle γ (°)	Lv et al. (*MPa*)	Sun and Gui (*MPa*)	Present study (*MPa*)
0.000	33.0	31.2	33.4
0.004	39.4	38.0	39.5
0.007	64.4	62.2	62.9
0.010	414.8	409.8	371.3

At the off-grid validation points, the component-wise regression coefficients were Kxx = 0.99809, Kxy = 0.99155, Kyx = 0.99950, Kyy = 0.99540, Cxx = 0.97745, Cxy = 0.99881, Cyx = 0.99910, and Cyy = 0.99993. The interpolation therefore retained the principal evolution of every coefficient.

Table S21. Component-wise regression consistency for off-grid interpolation.

Dynamic coefficient	R^2
Kxx, Kxy, Kyx, Kyy	0.99809, 0.99155, 0.99950, 0.99540
Cxx, Cxy, Cyx, Cyy	0.97745, 0.99881, 0.99910, 0.99993

No experimental critical-speed or unbalance-response data are currently available for the target three-disc, four-support rig. The present evidence must therefore not be described as a complete system-level experimental calibration. Its strength lies in independent checks of the key submodules, comparison of the structural modes with ANSYS, and direct off-grid agreement between the FSI calculations and database interpolation. Final system-level experimental validation remains future work.

S6 Modal mechanism underlying the local J4 stiffness increase and the weak sensitivity of low-order critical speeds

At 2884 *rpm*, the direct-stiffness trace at the loaded-end support J_4 increased from 2.6629×10^6 to 1.2514×10^8 $N\,m^{-1}$, a ratio of 46.9945, or approximately 47. The relevant system-level question is not the local multiplication factor itself, but the fraction of that boundary change that enters a branch through its modal projection.

Because M_r is a derived eccentricity-inclination descriptor rather than an interpolation variable, the physical end load F was used as the continuation parameter. From F = 0 to 30 N, the bearing coefficients were updated in 1 N increments and reconstructed by two-dimensional load-speed interpolation at every synchronous-root search speed. Modal identity between adjacent load states was maintained with the mass-weighted complex modal assurance criterion (*cMAC*):

$$cMAC(\phi_a,\phi_b)=\frac{\left|\phi_a^H M\phi_b\right|^2}{(\phi_a^H M\phi_a)(\phi_a^H M\phi_b)} \tag{S10}$$

The two intersections near 2.89 *krpm* belong to neighbouring *FW* and *BW* branches, not to one critical-speed branch. Continuous tracking gave endpoint changes of −0.0003695% and +0.0003885%, respectively.

Table S22. Continuous tracking of the neighbouring low-order synchronous branches.

Branch	Critical speed at F = 0 (*rpm*)	Critical speed at F = 30 N (*rpm*)	Change (%)	Minimum adjacent-state *cMAC*	Endpoint *cMAC*
FW	2883.6771	2883.6665	−0.0003695	0.999966	0.99978
BW	2894.9847	2894.9960	+0.0003885	0.999979	0.99996

Why, then, does a nearly 47-fold local increase at J_4 barely shift the low-order critical speeds? The eigenvalue response depends on the generalised projection of the local K/C change at the support, not on its local magnitude alone. For interpretation, the energy-type bearing-stiffness participation was evaluated with the symmetric part $K_i^s = \left(K_i + K_i^T\right)/2$ while the complete non-symmetric *K/C* matrices were retained in the eigenvalue calculation.

Table S23. Critical-speed sensitivity and support participation of the synchronous branches.

Branch	Critical-speed change (%)	η_K, low flexibility (%)	η_K, high flexibility (%)	η_u, low flexibility (%)	η_u, high flexibility (%)
FW	−0.0003695	0.061298	0.063788	0.002574	0.002565
BW	+0.0003885	0.16492	0.16929	0.006915	0.006952
H1	+0.014017	0.25919	0.20606	0.013987	0.011797
H2	+0.14771	1.4493	1.2858	0.056847	0.066313

The generalised bearing-stiffness participation of *FW* and *BW* was only approximately 0.061%-0.169%, and their bearing-location displacement participation was approximately 0.0026%-0.0070%. Their generalised stiffness therefore remained dominated by shaft bending. For *H2* in the low-flexibility state, η_K = 1.4493% and η_u = 0.056847%, approximately 23.6 and 22.1 times the corresponding *FW* values, while its critical-speed change reached 0.14771%. Identical support redistribution is consequently weighted very differently by the modal branches.

The endpoint *cMAC* values for *FW*, *BW*, *H1*, and *H2* all exceeded 0.998, showing that the global modal backbone was not substantially reconstructed. The higher sensitivity of *H2* therefore reflects stronger generalised coupling at the bearing locations rather than a change of modal identity.

For *FW*, replacing the J_4 stiffness alone produced a −0.005806% change, whereas the combined J_1-J_3 boundary change contributed +0.005156% in the opposite direction, reducing the complete response to −0.000370%. For *BW*, the isolated J_4 stiffness and damping contributions were +0.003112% and +0.007825%, but their non-additive *K-C* interaction was −0.008365%; the combined J_1-J_3 change further reduced the complete response to +0.000389%.

Only after support participation, multi-support compensation, and non-additive *K/C* interaction are considered does the apparent contradiction disappear. Local oil-film stiffening primarily suppresses motion and redistributes reactions near J_4. Only the small portion projected by a particular modal vector can shift that branch appreciably; the remainder is expressed through local constraint, reaction redistribution, or selective effects on branches with stronger support participation.

Table S24. Diagnostic finite-boundary replacement decomposition for the low-order *FW* and *BW* branches.

Boundary contribution	FW change (%)	BW change (%)
J_4 stiffness only	−0.005806	+0.003112
J_4 damping only	+0.000504	+0.007825
J_4 K–C non-additive interaction	−0.000590	−0.008365
J_1–J_3 combined boundary change	+0.005156	−0.002178
J_4 vs J_1–J_3 interaction	+0.000366	−0.000005
Complete *F*=0→30 boundary change	−0.000370	+0.000389